Linewidths in bound state resonances for helium scattering from Si(111)–(1 × 1)H

F E Tuddenham[1]**, H Hedgeland**[1]**, J Knowling**[1]**, A P Jardine**[1]**,**
D A MacLaren[2]**, G Alexandrowicz**[1,3]**, J Ellis**[1] **and W Allison**[1]

[1] Cavendish Laboratory, University of Cambridge, J J Thomson Avenue,
Cambridge CB3 0HE, UK
[2] Department of Physics and Astronomy, University of Glasgow, Glasgow G12 8QQ, UK

E-mail: fet22@cam.ac.uk

Received 28 November 2008
Published 11 June 2009
Online at stacks.iop.org/JPhysCM/21/264004

Abstract
Helium-3 spin-echo measurements of resonant scattering from the Si(111)–(1 × 1)H surface, in
the energy range 4–14 meV, are presented. The measurements have high energy resolution yet
they reveal bound state resonance features with uniformly broad linewidths. We show that exact
quantum mechanical calculations of the elastic scattering, using the existing potential for the
helium/Si(111)–(1 × 1)H interaction, cannot reproduce the linewidths seen in the experiment.
Further calculations rule out inelastic and other mechanisms that might give rise to losses from
the elastic scattering channels. We show that corrugation in the attractive part of the
atom–surface potential is the most likely origin of the experimental lineshapes.

(Some figures in this article are in colour only in the electronic version)

1. Introduction

Resonant scattering of atoms at surfaces occurs whenever the
incident wave is degenerate with a closed diffraction channel,
corresponding to motion parallel to the surface. In general,
resonant scattering causes sharp changes in the intensity
of the diffracted beams, which can be recorded readily in
experiment [1]. The energy and momentum dependence of
the features corresponds to the 2D band structure of atoms
confined to the near-surface region. In the case of a weakly
corrugated surface, the motion parallel to the surface can be
regarded as free-atom like and the kinematic conditions for
resonant scattering give simple, parabolic bands corresponding
to the mass of a helium atom. In this approximation,
the energy of particular resonances relates directly to the
functional form of the laterally averaged potential. Most
experimental studies, to date, have concentrated on the laterally
averaged potential and measurements have been used to test
and develop potentials for a number of surfaces [1–3]. Other
important aspects of the helium–surface potential, such as
the corrugation of the repulsive wall, are usually determined
from measurements of diffraction intensity. Thus the problem

of determining a helium–surface potential is divided neatly
into two separate experimental aspects: resonance scattering
measurements to give the laterally averaged potential and
diffraction experiments to give the repulsive corrugation. The
existing potential for scattering from Si(111)–(1 × 1)H was
determined in such a way [4]. In the present work, we show
that important aspects of the potential may be overlooked by
this naive separation of the potential into an uncorrugated
attractive well and a corrugated repulsive wall. Specifically, we
argue that the lineshape of features in the resonant scattering
indicates that a significant corrugation must be applied to
the attractive part of the potential, in order to model helium
scattering from the Si(111)–(1 × 1)H surface accurately.

We have used the helium-3 spin-echo technique [5] to
observe bound state resonances (BSRs) over a range of
energies. Helium-3 spin-echo is primarily used for measuring
surface dynamics, but used in the 'one-coil' configuration,
also known as Fourier transform helium atom scattering (FT-
HAS) [5–7], it has been used to study resonant scattering. The
Cambridge Helium-3 Spin-Echo Spectrometer, described in
detail elsewhere [8], provides a much higher energy resolution
than is possible with conventional, time-of-flight methods, and
allows the natural lifetime of the resonance to be observed.

The Si(111)–(1 × 1)H surface is an ideal system for
study since it is relatively stable and inert. The small size

---

[3] Present address: Schulich Faculty of Chemistry, Technion-Israel Institute of
Technology, Technion City, Haifa 32000, Israel.

of the unit cell facilitates computation of the scattering using an exact, close-coupling method [3, 9] and enables us to consider the most important factors that affect the lineshape of resonant features. Si(111)–(1 × 1)H is of particular current interest because of its potential application as an atom focusing mirror [10–12]. Using an *ex situ* wet etch technique it is now relatively straightforward to produce ultraflat Si(111)–(1 × 1)H surfaces of high quality for use in helium atom scattering experiments [10].

2. Experimental details

The Si(111)–(1 × 1)H sample was prepared from a thermally oxidized Si(111) surface [13], cut from a single crystal of flat-zone (FZ), n-doped silicon, with bulk oxygen content [O] = 4.5×10^{15} cm^{-3}. The surface was hydrogen passivated using a recently developed procedure [10], consisting of alternating stages of oxidation/cleaning in dilute piranha solution (a mixture of sulfuric acid and hydrogen peroxide) and oxide removal in hydrofluoric acid. A final etch in ammonium fluoride was used to smooth, flatten and hydrogen terminate the surface. The surface quality was characterized using atomic force microscopy (AFM) [10] and an AFM topographic image of an Si(111)–(1 × 1)H surface cut from the same crystal, prepared using this procedure, is shown in figure 1.

The topograph shows a wide area scan (2.5 × 2.5) μm^2 in which the main features are bilayer steps (∼0.38 nm) running across the figure, arising from the natural miscut of the surface. The steps themselves show a characteristic sawtooth profile that is consistent with the kinetically more stable, monohydride terminated [11$\bar{2}$] step orientation [14]. A small number of isolated, light protrusions with nanometre length scale can be seen in the figure, which correspond to particulate contamination. The low density of the features evident in figure 1 demonstrates that the surface is of a high quality. The topograph shows that, between the steps, the Si(111)–(1 × 1)H surface consists of large, atomically-flat terraces. Higher resolution scans show the terraces have a uniform contrast with very few defects, indicating that the surface processing is close to optimal [10].

To prevent surface degradation through exposure to ultraviolet light or atmospheric moisture during transfer of the sample to the spin-echo spectrometer, the final hydrogen passivation step and mounting procedure were carried out under nitrogen and in darkness [10]. The scattering chamber is equipped with an ion gauge and mass spectrometer for measuring the chamber pressure and sample reflectivity respectively. These were not used during the experiment, to avoid the possibility of surface degradation from the ionizing filaments [15]. After measurements had been completed, the scattering chamber pressure and the helium reflectivity were measured. The unbaked chamber pressure was 2×10^{-9} mbar and the absolute sample reflectivity was better than 1.5%. All measurements were carried out at room temperature.

The FT-HAS technique [5, 6] was applied to measure BSR features in the specular scattered helium beam. Using a beam with a broad spread of atom velocities, spin rotation scans were performed to generate high resolution energy distributions of
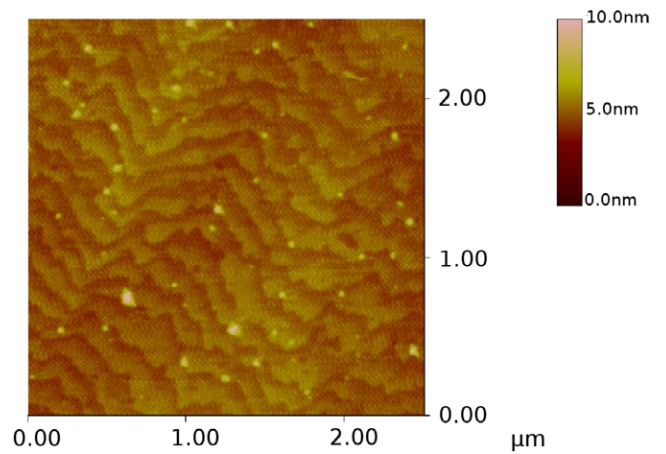
Figure 1. (2.5 × 2.5) μm^2 AFM image of hydrogen-passivated Si(111), prepared using an *ex situ* wet etch. Bilayer steps, travelling from bottom left to top right, can be seen in the image. The step density corresponds to the natural miscut angle of the sample, 0.1°. Other features of the image—terraces, oxidation and contaminants—are described in the text.

the specular scattered beam. The azimuthal dependence of the specular scattered intensity over an angular range of 40°, with fixed polar angle, $\theta = 22.2°$, was obtained by rotating the sample about the surface normal. At each azimuthal angle, two spin rotation scans were obtained: one for a mean incident beam energy of ∼8 meV and a second for ∼12 meV. Spin rotation scans were Fourier transformed to wavelength, then converted to an energy scale, to give an energy–intensity scan [5]. The scans consist of distinct maxima and minima, caused by resonant scattering, superimposed upon a broad Gaussian profile, which arises from the underlying velocity spread of the incident atoms. The broad background was extracted by smoothing the data. To normalize the scans to each other and extract the useful BSR information from the background, the following procedure was applied [7]. Each $I(E)$ scan was normalized by dividing by its maximum intensity and smoothed using a locally estimated scatter plot smoothing (LOESS) algorithm, to remove contributions from noise or BSRs. Each scan was then renormalized by dividing by the maximum of the smoothed version. Residuals of each data set were generated by subtracting from each renormalized scan the normalized, smoothed version. The result is a normalized set of scans, each consisting of a series of BSR maxima and minima on a flat background [7]. The low energy data and higher energy data, centred at ∼8 meV and ∼12 meV respectively, were combined by ignoring the weaker signal in the overlapping region; thus, 'cutting and joining'—taking the low energy residuals exclusively below a certain energy and the high energy residuals exclusively above this energy. An energy of approximately 9 meV was chosen as the 'joining point' as it lies in the region for which the high and low energy residuals are equal, thus minimizing discontinuities at the joining point, while eliminating the noisiest regions of the higher energy residuals.

198 $I(E)$ datasets were obtained over a period of about three weeks. During the course of the experiments there was a
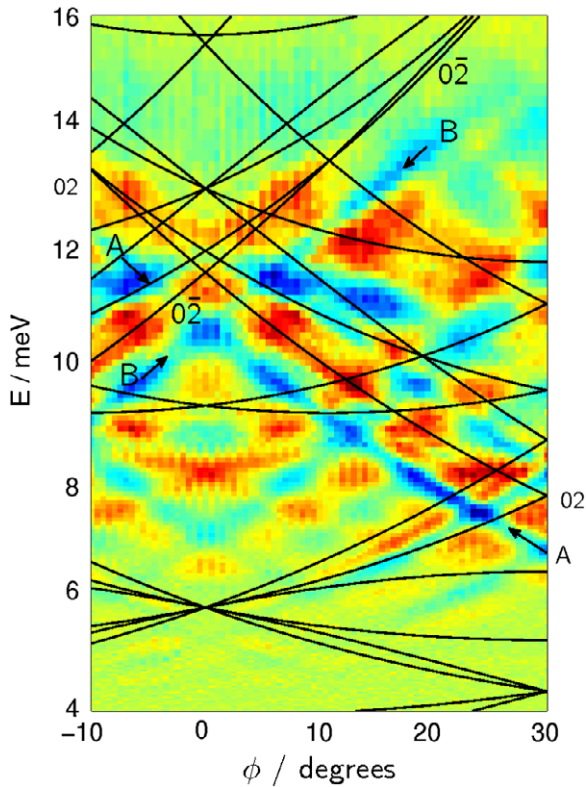
Figure 2. Experimental results, showing the specular intensity, coded as colour, as a function of incident energy and azimuthal angle, ϕ, from the [11$\bar{2}$] azimuth. Measurements were taken with an angle of incidence $\theta = 22.2°$, and at a surface temperature of 290 K. Individual datasets were normalized and combined as described in the text. The colour scale runs from blue at low intensity, to red at high intensity. Free-atom diffraction thresholds are shown in black. The BSR dispersion is predominantly free-atom like. For example, features A and B run almost parallel to the (02) and (0$\bar{2}$) thresholds, respectively.

decrease in specular scattered intensity, which can be attributed to gradual surface contamination [16]. The normalization procedure corrects for variations in the overall reflectivity and comparisons between spectra taken at different stages showed that the shape of the resonance peaks and dips did not vary with time. We conclude that contamination was not sufficient to affect the behaviour of bound state atoms.

3. Results

Reflectivity data, after normalization, is shown in figure 2. The intensity scattered in the specular direction is presented in a colour plot as a function of both incident energy and azimuthal angle. Green regions correspond to the mean, local reflectivity, yellow and red regions show enhanced scattering while blue features correspond to a reduction in the scattered intensity. Features appear strongest where the beam intensity is highest, in the region between 6 and 14 meV. Plotting the full set of data in this way makes the dispersion of the resonances clear, even in the noise-dominated tail of the energy distribution, at energies as low as 4 meV.

The features disperse with energy and, to aid comparison with free-atom dispersion, all the kinematically allowed
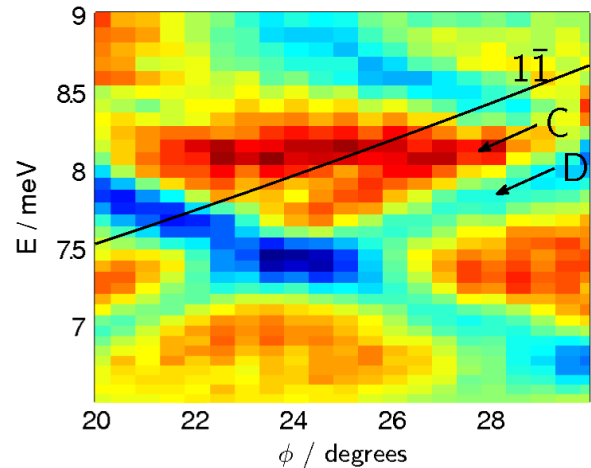
Figure 3. Expanded region of figure 2, showing the region close to the (1$\bar{1}$) threshold. The maxima and minima, labelled C and D, are both possible candidates for a BSR associated with (1$\bar{1}$), corresponding to energies -0.25 meV and -0.50 meV, respectively.

resonance thresholds are shown as solid lines in figure 2. Features (maxima or minima) that lie below and nearly parallel to a threshold can be attributed to free-atom like states associated with that particular threshold. For example, two prominent minima in figure 2 have been labelled A and B. They run almost parallel to the (02) and (0$\bar{2}$) diffraction thresholds respectively.

A striking feature of the data in figure 2 is that the BSR structures are broad, with widths that are significantly greater than the experimental resolution. Previous measurements, at high energy resolution, for the lithium fluoride surface [6], which has a similar corrugation to that of the existing potential for Si(111)–(1 × 1)H [4], showed many narrow features that could be assigned to specific bound state energies within the free-atom model. In contrast, the broad features in figure 2 introduce a degree of ambiguity into the process of identifying resonances and their associated bound state energies. Figure 3 illustrates one of the difficulties in assigning BSRs. It shows, in an enlarged form, the region below the (1$\bar{1}$) diffraction threshold. The maxima and minima labelled C and D, directly below the threshold, correspond to free-atom bound states associated with (1$\bar{1}$) at -0.25 meV and -0.50 meV respectively. These could be interpreted as two separate resonances, corresponding to two separate bound states. Alternatively, the two features could be interpreted as the peak–dip or dip–peak series of a single Fano-type resonance, in which case there is uncertainty in assigning the position in energy which corresponds to the bound state energy.

When attempting to assign the resonances in the data as maxima or minima, we have found that it is impossible to obtain a single, consistent set of energy values that correspond to eigenstates of a laterally averaged potential. It follows that the free-atom approximation is an inadequate starting point for any analysis of the potential. We are faced with the interesting paradox that the features disperse like free-atom states yet they cannot easily be ascribed to particular bound states within the free-atom approximation.

In order to explore the apparent paradox in more detail we take the existing potential [4] as a reference point for calculations and consider various approaches to understand the data.
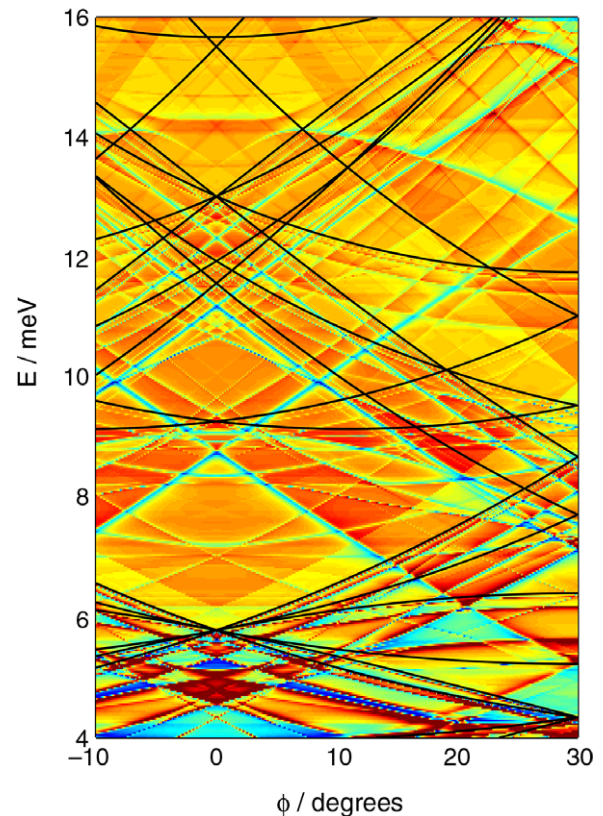
4. Scattering calculations

We have used the close-coupled method [9] to calculate resonance features over the same energy and momentum range as in the experiment. The method gives a solution to the Schrodinger equation, by expanding the helium atom wavefunction and surface potential as Fourier series, then solving the subsequent coupled equations. It avoids the need to invoke the free-atom approximation, so can be regarded as exact. The iterative method of solution implemented by Manolopoulos and Wyatt [17] was employed. We use up to 50 diffraction channels, both open and closed, and an integration range of $z = 0.5$–25 Å to achieve convergence in the results.

We begin with the results for the existing potential [4], which may be regarded as the reference potential for the later discussion. The calculations are shown in figure 4. Here, the colour corresponds to the calculated specular scattering intensity as a function of incident energy and azimuthal angle; however, unlike figure 2, the data is shown as an absolute intensity scale with blue representing low intensity and red high intensity. As before, all of the relevant diffraction thresholds are included as bold lines in the figure. Most features in figure 4 can be seen to follow the dispersion of the associated diffraction threshold and, in this sense, the calculations agree with the observations. Furthermore, it is a straightforward matter to ascribe the calculated features below each threshold to a consistent set of bound states of the laterally averaged potential. Inspection of the calculated spectra (figure 4) and experiment (figure 2) shows that the key difference between them lies in the width of the BSR features. Calculated BSRs, such as the strong minima (diagonal, blue features), are much narrower than any of the features observed in the experiment (figure 2). Narrow resonances are associated with states having a long lifetime [3] and we conclude that the lifetime of states in the experiment is significantly shorter than the natural lifetime of those supported by the existing potential.

In order to reconcile the experiment with the calculation, we have considered the various factors that affect and limit the lifetime of resonant states. For purely elastic scattering, the lifetime is limited only by the probability of scattering out of the bound state channel, which relates to the precise form of the lateral corrugation in the atom–surface potential. If the particle can undergo inelastic scattering, the natural lifetime can be reduced by factors such as defect or phonon scattering. Before returning to the question of the corrugation we explore, and rule out, effects due to such inelastic scattering.

Defect and phonon scattering correspond to loss of flux from the elastic scattering channels. We have modelled the loss using an optical potential [18, 3]. Optical potentials have been used previously to study the effect of inelasticity on resonance scattering for lithium fluoride (001) and sodium fluoride (001) [19], graphite (0001) [20–22] and nickel (110) [23]. In the present work, phonon scattering is modelled by an

Figure 4. Specular intensity calculated for scattering from the reference potential [4], as a function of incident energy and azimuthal angle, and constant polar angle $\theta = 22.2°$. The free-atom diffraction thresholds are shown as black lines. Specular scattered intensity is shown as background colour on an absolute intensity scale with blue representing low intensity and red high intensity.

imaginary term in the potential, proportional to the gradient of the laterally averaged well close to the surface. The resulting function is localized in the repulsive potential wall, where phonon interaction occurs, and increases strongly as the atoms at the surface are approached. Defect scattering is modelled by an imaginary term that is Gaussian in form, with width ∼0.5 Å localized 1.5 Å above the centre of the surface atoms. The form is chosen to model a single atomic scale defect, such as a silicon atom terminated by something other than a hydrogen atom, or an isolated contaminant atom physisorbed at the surface. An overall scaling factor for each imaginary term allows the magnitude of the effect to vary in order to simulate a given loss of flux.

Figure 5 shows the specular intensity calculated for scattering from the reference potential with the imaginary potential included. Data is shown for a range of polar angles, θ, at a fixed energy, $E = 20$ meV, and azimuth, $\phi = 30°$. The conditions are chosen to illuminate a sequence of five isolated BSRs. Figure 5(a) shows the results of using the model for phonon scattering, while figure 5(b) shows the case for defect scattering. In both cases, the topmost curve corresponds to purely elastic scattering and the other curves are generated by progressively increasing the imaginary part of the potential. As the loss from the elastic channels increases, the results show the expected decrease in the elastically scattered signal.
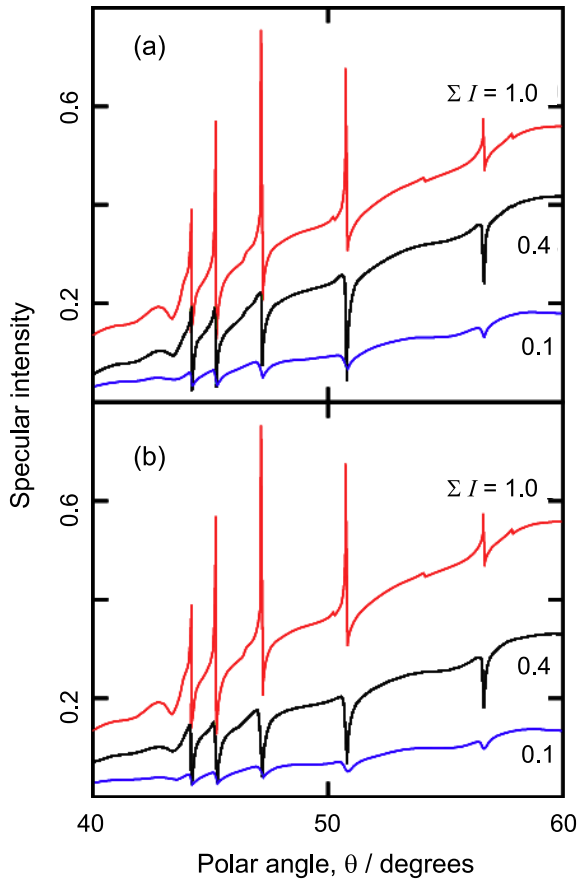
Figure 5. The effect of scattering from an optical potential, calculated as a function of polar angle, θ, for fixed incident energy $E = 20$ meV and azimuthal angle $\phi = 30°$, for a sequence of five isolated resonances. The top curve is for purely elastic scattering ($\Sigma I = 1$). The lower curves correspond to inelastic losses of 60% and 90%, leaving outgoing flux 40% and 10%, respectively. (a) shows phononic scattering, modelled by an imaginary function proportional to the gradient of the laterally averaged well close to the surface. (b) shows defect scattering, modelled by an imaginary Gaussian of atomic width at the surface.

Simultaneously, the BSR features are broadened, though only slightly, and they become drastically smaller in amplitude. Neither model offers a viable explanation for the linewidth of the experimental data. Even in the extreme case where 90% of the scattering is inelastic, or lossy (lowest curves in figure 5), the BSRs retain their identity as isolated resonances and have linewidths significantly less than those observed in the experiment.

Having ruled out the possibility of inelastic scattering, we return to the question of the resonance lifetime within the context of purely elastic scattering. The lifetime can only be reduced by increasing the scattering rate out of the resonant state, which would conventionally be achieved by increasing the lateral corrugation of the potential [3]. However, the extent to which the corrugation of the reference potential can be increased is limited, since it was determined by fitting to diffraction intensities from a separate experiment performed at higher energies [4]. A potential with significantly increased corrugation is unlikely, therefore, to accurately describe

diffraction from the Si(111)–(1 × 1)H surface. In the original study [4], the diffraction experiments were analysed using a potential model in which the corrugation terms are purely repulsive, and as a result, the corrugation of the reference potential is confined exclusively within the repulsive wall of the potential.

The non-zero Fourier components of the reference potential have the form [4]

$$V_G = A_G e^{-B_G z}, \qquad (1)$$

where V_G is the Fourier component associated with reciprocal lattice vector G. The lateral corrugation at 20 meV is 0.620 Å, with the main contribution arising from the two lowest order non-zero components, (10) and (21). We have assessed the extent to which these corrugation amplitudes can be increased by examining how the diffraction intensities change as the reference potential [4] is modified. The corrugation was modified by changing the decay constants associated with the (10) and (21) Fourier components, B_{10} and B_{21} respectively, since these parameters have the greatest effect on the corrugation. A χ^2 parameter allows the calculated intensities, for the modified potential, to be compared with those of the reference potential. Thus, the minimum value of χ^2, when the reference potential is compared with itself, is identically zero. For incident conditions we used an energy of $E = 20$ meV, polar angle $\theta = 30°$ and azimuthal angle $\phi = 0°$, taking 16 non-symmetric diffraction intensities in the χ^2 sum. The results are shown in figure 6. The figure shows the corrugation (coded as colour), together with the fit to diffraction data, χ^2, as a function of the fractional change in B_{10} and B_{21}. The colour scale for the corrugation of the potential, calculated at 20 meV, ranges from high corrugation in red to low corrugation in blue. We use the χ^2 data to define a maximum corrugation that is still consistent with the diffraction data by taking the contour at $\chi^2 = 0.64$. This corresponds to diffraction intensities that vary by approximately 20% from those of the reference potential. The allowable parameter sets lie within this contour, which is the innermost contour (emboldened for clarity) of figure 6. The maximum corrugation in this region is 0.636 Å, only 3% higher than the corrugation of the reference potential. Calculations using the modified potential with this corrugation give rise to a band structure which is essentially identical to figure 4, and the slight increase in corrugation, while having a significant effect on diffraction intensities, is insufficient to cause any noticeable resonance broadening. Thus, the corrugation of the repulsive wall cannot be increased whilst still adequately describing diffraction from the surface. It follows that a different source of corrugation is required.

We now investigate the effect of a corrugated attractive region. Manson and Rieder have shown that corrugating the attractive part of a potential has little effect on diffraction intensities, compared to the effect of the repulsive corrugation [24]. However, a corrugated well may have a greater effect on the resonance lifetimes. We use a corrugated Morse potential [3, 25] as it provides the correct attributes for corrugating the attractive part of the well, combined with a convenient functional form. The specular intensity for
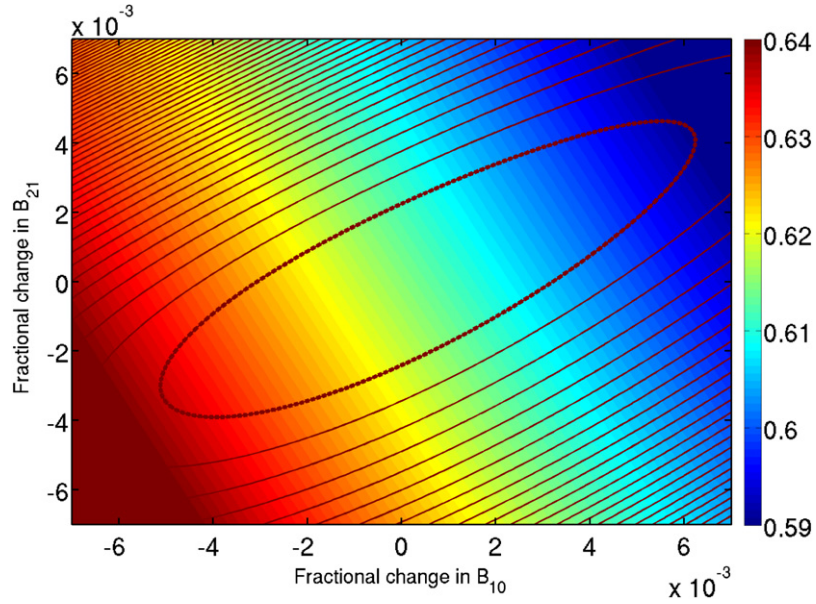
Figure 6. The effect of varying the reference potential Fourier component decay constants, B_{10} and B_{21}, on the calculated diffraction intensities for incident energy, $E = 20$ meV, polar angle, $\theta = 30°$, azimuthal angle, $\phi = 0°$. Background colour corresponds to the corrugation of the 20 meV energy contour, with the scale given by the colour bar. Overlaid are contours of constant χ^2 between the 16 calculated diffraction intensities and those of the original potential. The central contour corresponds to $\chi^2 = 0.64$, and the contour value increases in intervals of 0.64 moving outwards. The emboldened innermost contour encloses the allowable parameter sets consistent with data for diffraction from the surface [4], if we assume that a variation of 20% in diffraction intensities is acceptable.

scattering from the reference potential is compared with that from the Morse potential in figure 7. Parameters in the Morse potential were chosen to give as close a correspondence between the two potentials as possible. In particular, the corrugation of the repulsive wall was adjusted to be the same as the reference potential, at the 20 meV contour, and the laterally averaged potential adjusted to support similar bound state energies. The intensity is calculated in a region where three isolated resonances appear, all related to the (02) diffraction channel. The upper panel in figure 7 shows calculations for the reference potential, while the lower panel shows the corresponding results for the corrugated Morse potential. Both panels show three features; however, the lineshapes are dramatically different. Whereas the reference potential shows narrow, well-defined resonances, the widths of the broad features arising from the Morse potential are comparable to the linewidths of the resonances seen experimentally.

The enhancement to the linewidth, evident in figure 7, can be considered quantitatively using the mixed S-matrix method [3, 26, 27]. For an isolated resonance, the imaginary part of the resonance profile as a function of the dynamical variable, α, is related to scattering matrix by

$$I(\alpha) = \text{Im}(\text{Tr}[S_{\text{bg}}^{\dagger} S]) = -\frac{\Gamma(\alpha - \bar{\alpha})}{(\alpha - \bar{\alpha})^2 + \frac{\Gamma^2}{4}}, \qquad (2)$$

where $\bar{\alpha}$ and Γ are the resonance position and width respectively. S is the full scattering matrix and S_{bg} the background scattering matrix. We calculate S_{bg} by allowing all non-resonant channels to vary normally over the resonance region, but fixing the resonant channel at its non-resonant value [27]. The resonance position, $\bar{\alpha}$, is then given by the

Table 1. Linewidths and positions of the resonances shown in figure 7, determined quantitatively using the mixed matrix method described in the text. The resonances are all associated with the (02) diffraction channel. n refers to the energy level of the associated bound state. The resonances supported by the corrugated Morse potential are between 7 and 20 times wider in θ than those of the reference potential.
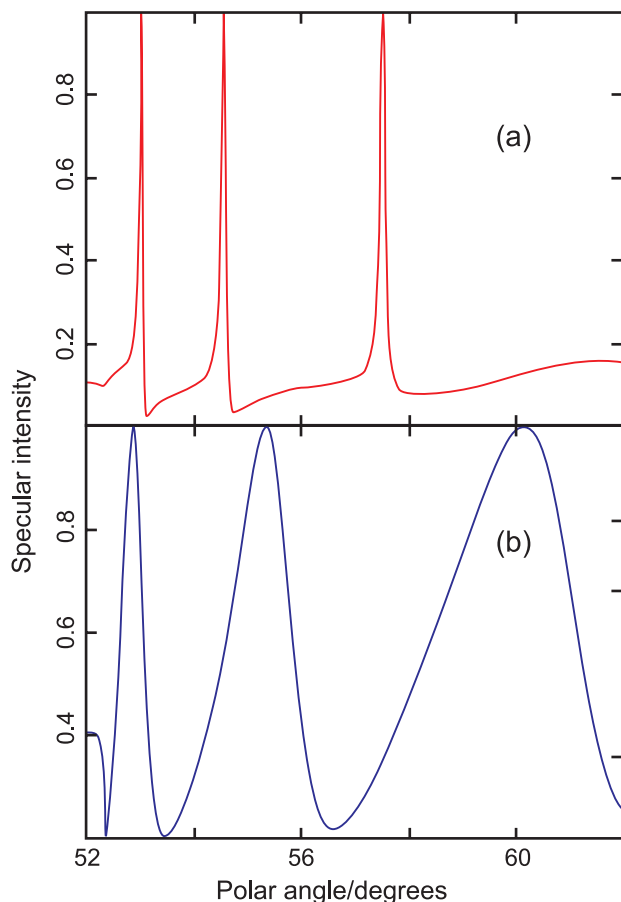
	Morse potential		Reference potential	
n	Position	Width	Position	Width
4	52.90°	0.40°	52.95°	0.06°
3	55.48°	1.11°	54.56°	0.09°
2	60.48°	2.29°	57.53°	0.12°

root of equation (1), while the width, Γ, follows from the separation of the extrema. Table 1 shows the results for the data in figure 7. It can be seen that the resonance widths for the corrugated Morse potential are between 7 and 20 times greater than for the reference potential even though the kinematic conditions in the two cases are almost identical.

The dramatic broadening induced by the corrugated Morse potential appears to offer a better representation of the experimental data than the reference potential.

5. Discussion and conclusion

The calculations in section 4 have demonstrated that the new measurements of resonance linewidths cannot be explained simply by the effects of inelastic or defect scattering. Therefore, the observed behaviour must arise, predominantly, from elastic scattering. It is also evident that small changes to the corrugation of the repulsive wall do not provide a

Figure 7. Specular intensity calculated for scattering from the reference potential (a) and the corrugated Morse potential described in the text (b). Scattered intensity is calculated as a function of θ for fixed energy 20 meV and azimuthal angle $\phi = 30°$. The three resonances shown are associated with the (02) diffraction channel.

qualitative, and much less a quantitative, description of the experimental results. In contrast, a Morse potential with the same corrugation gives features whose linewidth is similar to those seen in the experiment.

The functional form of the Morse potential cannot model the helium–surface van der Waals interaction adequately, and so further quantitative analysis based upon the Morse potential would have little value. Figure 8 compares potentials and illustrates the important feature of the corrugated Morse potential, namely the magnitude of the corrugation in the attractive region. The two potentials have been shifted laterally so that the classical turning point at 20 meV is at the origin in z, marked with a cross, in the upper panel, figure 8(a). The lower panel, figure 8(b), overlays curves for the lowest order periodic Fourier component, which dominates the corrugation in both cases. The magnitude of the corrugation in the two curves is the same at the matching point, as can be seen in the lower panel at $z = 0$. Note, however, that the corrugation of the Morse potential (solid line) decreases much more slowly with z and it extends throughout the region of the well to approximately 2 Å, unlike that for the reference potential (dashed line), which is confined to the region of the repulsive wall. We conclude that it is the greater corrugation in the attractive region of the
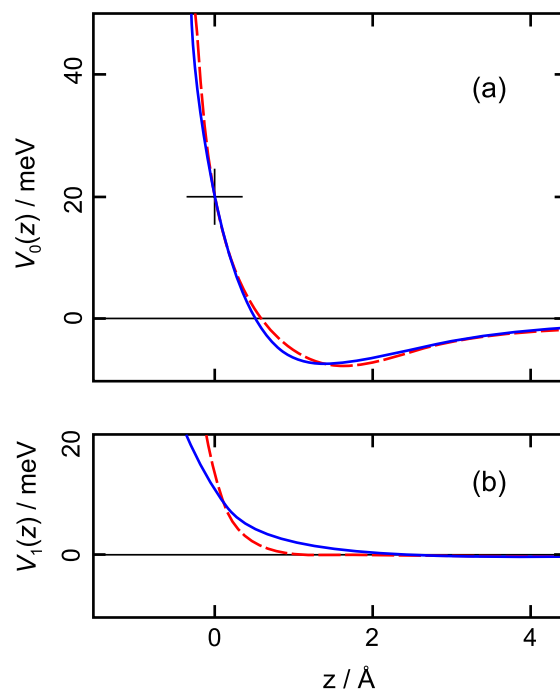
Figure 8. The laterally averaged well (a) and first periodic Fourier component (b) of the reference potential (dashed line) and corrugated Morse (solid line). The Morse potential corrugation has been determined by matching to the corrugation of the reference potential at $E = 20$ meV. To ease comparison, the potentials have been shifted rigidly in z to give the same classical turning point at 20 meV, where the corrugations were matched, indicated by the cross in the upper panel.

potential that gives rise to the broad resonance features seen in figure 7(b).

The results and analysis in the present work demonstrate that it is naive to assume that the atom–surface potential can be determined by a simple separation into a corrugated repulsive wall and an uncorrugated attractive well. We conclude that, in the interaction of helium with the Si(111)–(1 × 1)H surface, a significant corrugation exists in the region of the attractive well. That corrugation does not manifest itself strongly in the diffraction intensities since previous work [4] obtained a good fit to diffraction measurements without the inclusion of a corrugated well. Measurements of the type shown in the present work, which give information on the lineshape in resonant scattering, appear to offer insights into the potential that are not available from other experiments.

Acknowledgments

References

[1] Hoinkes H and Wilsch H 1992 *Helium Atom Scattering from Surfaces* ed E Hulpke (Berlin: Springer) chapter 7, pp 113–72

[2] Farias D and Rieder K 1998 *Rep. Prog. Phys.* **61** 1575–664
[3] Sanz A S and Miret-Artés S 2007 *Phys. Rep.* **451** 37–154
[4] Buckland J R and Allison W 2000 *J. Chem. Phys.* **112** 970–8
[5] Alexandrowicz G and Jardine A P 2007 *J. Phys.: Condens. Matter* **19** 305001
[6] Riley D J, Jardine A P, Dworski S, Alexandrowicz G, Fouquet P, Ellis J and Allison W 2007 *J. Chem. Phys.* **126** 104702
[7] Riley D J, Jardine A P, Alexandrowicz G, Hedgeland H, Ellis J and Allison W 2008 *J. Chem. Phys.* **128** 154712
[8] Fouquet P, Jardine A P, Dworski S, Alexandrowicz G, Allison W and Ellis J 2005 *Rev. Sci. Instrum.* **76** 053109
[9] Wolken G 1973 *J. Chem. Phys.* **58** 3047–64
[10] Barredo D, Calleja F, Weeks A E, Nieto P, Hinarejos J J, Laurent G, Vazquez de Parga A L, MacLaren D A, Farias D, Allison W and Miranda R 2007 *Surf. Sci.* **601** 24–9
[11] Holst B and Allison W 1997 *Nature* **390** 244
[12] Barredo D, Calleja F, Nieto P, Hinarejos J J, Laurent G, Vazquez de Parga A L, Farias D and Miranda R 2008 *Adv. Mater.* **20** 3492
[13] Surma B, private communication, Institute of Electronic Materials Technology, Warsaw
[14] MacLaren D A, Curson N J, Atkinson P and Allison W 2001 *Surf. Sci.* **490** 285–95
[15] Yun S J, Lee S C, Lee J J and Lee J Y 1996 *J. Vac. Sci. Technol.* A **14** 3189–93
[16] Doak R B, Chabal Y J, Higashi G S and Dumas P 1990 *J. Electron Spectrosc. Relat. Phenom.* **54/55** 291–8
[17] Manolopoulos D E, Wyatt R E and Clary D C 1990 *J. Chem. Soc. Faraday Trans.* **86** 1641–8
[18] Baz' A, Zel'dovich Y B and Perelomov A M 1966 *Scattering, Reactions and Decay in Nonrelativistic Quantum Mechanics* (Jerusalem: Israel Program for Scientific Translations)
[19] Chow H and Thompson E D 1979 *Surf. Sci.* **82** 1–21
[20] Wolfe K L and Weare J H 1980 *Surf. Sci.* **94** 581–92
[21] García N, Carlos W E, Cole M W and Celli V 1980 *Phys. Rev.* B **21** 1636–46
[22] Wolfe-Brannon K and Weare J H 1981 *Phys. Rev.* B **24** 5753–62
[23] Liebsch A and Harris J 1981 *Surf. Sci.* **111** L721–7
[24] Manson J R and Rieder K H 2000 *Phys. Rev.* B **62** 13142–6
[25] Gorse D, Salanon B, Fabre F, Kara A, Perreau J, Armand G and Lapujoulade J 1984 *Surf. Sci.* **147** 611–46
[26] Delgado-Barrio G, Villarreal P, Mareca P and Beswick J A 1985 *Int. J. Quantum Chem.* **27** 173–80
[27] Hernandez M, Miret-Artés S, Villarreal P and Delgado-Barrio G 1992 *Surf. Sci.* **274** 21–34